

## REPORT DOCUMENTATION PAGE

Form Approved  
OMB NO. 0704-0188

Public Reporting burden for this collection of information is estimated to average 1 hour per response, including the time for reviewing instructions, searching existing data sources, gathering and maintaining the data needed, and completing and reviewing the collection of information. Send comment regarding this burden estimate or any other aspect of this collection of information, including suggestions for reducing this burden, to Washington Headquarters Services, Directorate for Information Operations and Reports, 1215 Jefferson Davis Highway, Suite 1204, Arlington, VA 22202-4302, and to the Office of Management and Budget, Paperwork Reduction Project (0704-0188), Washington, DC 20503.

1. AGENCY USE ONLY (Leave Blank)		2. REPORT DATE 6/12/99	3. REPORT TYPE AND DATES COVERED Final Report, 6/93-6/96
4. TITLE AND SUBTITLE Fiber-Optic Chameleonic Skin		5. FUNDING NUMBERS DAAH04-93-G-0324	
6. AUTHOR(S) Michael L. Myrick			
7. PERFORMING ORGANIZATION NAME(S) AND ADDRESS(ES) Sponsored Programs and Research University of South Carolina, Columbia, SC 29208		8. PERFORMING ORGANIZATION REPORT NUMBER	
9. SPONSORING / MONITORING AGENCY NAME(S) AND ADDRESS(ES) U. S. Army Research Office P.O. Box 12211 Research Triangle Park, NC 27709-2211		10. SPONSORING / MONITORING AGENCY REPORT NUMBER ARO 32113.1-PH-SM	
11. SUPPLEMENTARY NOTES The views, opinions and/or findings contained in this report are those of the author(s) and should not be construed as an official Department of the Army position, policy or decision, unless so designated by other documentation.			
12 a. DISTRIBUTION / AVAILABILITY STATEMENT Approved for public release; distribution unlimited.		12 b. DISTRIBUTION CODE	
13. ABSTRACT (Maximum 200 words)  The purpose of this project has been to investigate fiber-optic array methods for creating and/or recording spectroscopic image information, plus rapidly manipulating this optical content for applications in optical camouflage. Our major investigations during this program have been for the creation of spealized dimension-transformation fiber-optic arrays and the development of techniques for interpreting multidimensional spectroscopic images (2-D and 3-D).			
14. SUBJECT TERMS fiber optics, fluorescence, multidimensional spectroscopy, optical computing, chemometrics, pattern recognition.			15. NUMBER OF PAGES 36
			16. PRICE CODE
17. SECURITY CLASSIFICATION OR REPORT UNCLASSIFIED	18. SECURITY CLASSIFICATION ON THIS PAGE UNCLASSIFIED	19. SECURITY CLASSIFICATION OF ABSTRACT UNCLASSIFIED	20. LIMITATION OF ABSTRACT UL

NSN 7540-01-280-5500

Standard Form 298 (Rev.2-89)  
Prescribed by ANSI Std. Z39-18  
298-102

DTIC QUALITY INSPECTED 4

19991101 132

## **Final Report**

ARO Grant DAAH04-93-G-0324

### **Fiber Optic Chameleonic Skin**

Principal Investigator: Michael L. Myrick  
Department of Chemistry and Biochemistry  
University of South Carolina  
Columbia, SC 29208

## **Table Of Contents**

<b>Memorandum of Transmittal.....</b>	<b>1</b>
<b>Title.....</b>	<b>2</b>
<b>Table of Contents. ....</b>	<b>3</b>
<b>List of Illustrations.....</b>	<b>4</b>
<b>Statement of the Problem Studied.....</b>	<b>5</b>
<b>Summary of the Most Important Results.....</b>	<b>6</b>
<b>List of Publications and Reports. ....</b>	<b>20</b>
<b>List of Participating Scientific Personnel. ....</b>	<b>24</b>
<b>Inventions. ....</b>	<b>25</b>
<b>Bibliography.....</b>	<b>26</b>
<b>Figures. ....</b>	<b>29</b>
<b>Form 298. ....</b>	<b>36</b>

## List of Illustrations.

- Figure 1.** White-light illuminated image of the two dimensional side of the fiber array magnified with an Optizoom microscope (Digital Instruments).
- Figure 2.** A Princeton Instruments ICCD camera image of the 544 x 1 distal end of the array taken with the zero-order grating reflection before (A) and after (B) vignetting and curvature correction.
- Figure 3.** (A) Illustration of the letter "A" used to "fine-tune" the pixel values; (B) A "blurred" image of the letter "A" showing the amount of image fidelity that would be expected for our system; (C) A reconstructed zero-order gray-scale image of the letter "A" demonstrating the level of image fidelity we have been able to achieve with our experimental set-up.
- Figure 4.** A first-order reconstructed gray-scale intensity image of the 722.9 nm emission line of lead generated from a single column of an ICCD image.
- Figure 5.** Side view schematic of the imaging spectrofluorometer illustrating the spatial relationship between the excitation optics and the sample.
- Figure 6:** The estimated lamp intensity profile as a function of wavelength (solid) calculated by ratioing the fluorescein fluorescence excitation profile (dashed) to the fluorescein absorbance spectrum (dotted).
- Figure 7:** Untreated negative EEM image of the instrumental background measured from ocean water blank (60 sec. exposure).

### **Statement of the Problem Studied**

The purpose of this project has been to investigate fiber-optic array methods for creating and/or recording spectroscopic image information, plus rapidly manipulating this optical content for applications in optical camouflage. Our major investigations during this program have been for the creation of specialized dimension-transformation fiber-optic arrays and the development of techniques for interpreting multidimensional spectroscopic images (2-D and 3-D).

## Summary of the Most Important Results

As a result of this work, we have developed a technique for manufacturing high-density fiber-optic arrays suitable for single-measurement spectroscopic imaging. We have also developed software for rapidly converting the output of these arrays into meaningful information content via pattern recognition procedures implemented in software. In addition, we have developed rapid instrumentation and analysis tools for multidimensional fluorescence suitable for the analysis of water and air samples for their biological and chemical content. Finally, we have developed a theory to underlie the pattern-recognition-based determination of environmental spectroscopy using a solid-state optical computation method. In summary, our developments are:

- manufacture of high-density fiber arrays for single-measurement imaging spectroscopy.
- software for rapidly deconvolving array output into its underlying spectroscopic patterns.
- multidimensional fluorescence-based instrumentation and software tools for air and water chemical analysis.
- theory for optical computation of environmental spectroscopic patterns.

### Summary 1.

#### Manufacture of high-density fiber arrays.

**Concept.** A number of approaches to the orderly construction of the array were contemplated and some approaches were attempted without success before a working concept was developed. Most of the failed ideas were defeated by the thinness of the fiber ribbons, and the inability of common machine tools to fabricate components with accuracies of  $<0.001$  in. Our approach to construction was to fabricate the rectangular proximal end of the array first, then proceed to the linear distal end, as outlined below.

Fiber ribbons consisting of 32 square  $25\text{ }\mu\text{m}$  cross-sectional  $f/2$  optical fiber waveguides were obtained from Collimated Holes Inc. of Campbell, CA. Construction of the proximal array end composed of 19 fiber ribbons proceeded by stacking each ribbon on top of one another and gluing them into an ST-type connector (Fiber Instruments Sales, Inc.) to enable coupling of an endoscope for future experiments.

Figure 1 shows a white-light illuminated image of the two dimensional side of the fiber array magnified with a Optizoom microscope (Digital Instruments). Note that there are 19 ribbons with 32 waveguides per ribbon. Since the Princeton Instruments ICCD had only 576 vertical imaging elements, only 17 of the 19 ribbons could be imaged from the one dimensional end at a time taking into account the unintended spaces between ribbons as a result of construction constraints. Note also a slight skew to the stack of ribbons which was probably caused by slight shifting during glue drying. The dimensions of the two dimensional end is approximately  $0.5\text{ mm} \times 0.75\text{ mm}$  making the amount of skew only about  $50\text{ }\mu\text{m}$ . The space occupied by Instant Adhesive 10-128 (a cyanoacrylate ester produced by GC electronics) between ribbons is no more than 2 or  $3\text{ }\mu\text{m}$  in most places.

Fabrication of the linear end of the array followed by first separating adjacent fiber ribbons, then twisting and orienting each so that neighboring ribbons on the  $19 \times 32$

proximal end were juxtaposed in the 608 x 1 linear array end. The purpose of this was to ensure that adjacent fibers in the linear end were also always adjacent on the rectangular end so that crosstalk would have a minimal impact on the final reconstructions. The linear end of the array was then glued with 5 Minute<sup>®</sup> Epoxy (Devcon Corp.) to a small piece of aluminum which subsequently became a permanent fixture in the final array assembly. Once the array was secured in its final mount, the ends were polished.

Figure 2A shows a Princeton Instruments ICCD camera image of the 544 x 1 distal end of the array taken with the zero-order grating reflection. The vertical axis corresponds to fiber position in the 544-element array, while the horizontal corresponds to the spatial dispersion direction. Figure 2A shows the same Princeton Instruments ICCD camera image as Figure 2B corrected for vignetting and curvature.

**Mechanical supports.** To facilitate the construction of the array, a series of tools were designed and constructed. A general description of these tools, without which the construction of the array could not have been completed, and their purposes are provided below. Engineering drawing and full details are available upon request. The parts were:

1. A mounting block (block A) for the proximal (rectangular) end of the fiber array was constructed to facilitate work with fiber ribbons of such small dimensions (approximately 4 x 0.032 x 0.001 in.) by providing a sharp interior corner into which the fibers could be stacked. The precision of the tools used to construct this mounting block were no more precise ( $\pm 0.001$  in.) than the smallest dimension of each ribbon, so the necessary sharpness in the angle could not be achieved by simply cutting metal into the required shape. Instead, we machined two pieces of aluminum, assembling the two in such a manner that a flat side of one was perpendicular to the flat side of the other, creating a 90° interior edge that could be used to precisely stack fiber ribbons. These parts were assembled under compression after deburring to prevent gapping.
2. A sliding press was machined from a piece of nylon stock to press the fibers firmly into the interior edge of block A.
3. A second mounting block (block B) was constructed to facilitate the fabrication of the linear end of the fiber array. Block B itself was composed of seven essential parts:
  - (a) a metal base (base B),
  - (b) a clamp to secure the ST-connector holding the glued two-dimensional end while configuring the one-dimensional end,
  - (c) a comb-like structure (the "comb") to separate individual fiber ribbons,
  - (d) a set of teeth-like clamps (the "dentures") to orient the strands of the ribbon into the serpentine form,
  - (e) a sliding aluminum arm on rails (the "compressor") to press the ribbons flat,
  - (f) a soft clamp (the "squeegee") to prevent movement of fibers once oriented, and
  - (g) a jack lift fitted with a small machined aluminum strip (the "jack and strip") to which the fiber ribbons were glued.

**Fiber preparation.** Fiber ribbons used in the assembly were prepared as follows. Four inch lengths of ribbon were cut with ordinary scissors and set aside taking special care to ensure that adjacent lengths were juxtaposed in the final construct in the event that

deviations in ribbon dimensions occurred as the fibers were drawn. Each length of fiber was then cleaned of debris by ultrasonication in an ethanol bath just prior to use.

**Assembly procedure.** The two dimensional end of the fiber array was constructed as follows. First, the ribbons were stacked one by one into the 90° edge of block A to create the proximal end of the array. Second, a drop of Instant Adhesive 10-128 was applied to the end of the fibers. Third, the dried fiber ribbon stack was then carefully mounted into an ST-type fiber-optic connector..

The linear end of the fiber array was constructed as follows. First, the fiber ribbons were then separated into adjacent grooves of the comb. Second, a specially-designed compression system was used to orient the fibers and align them. Third, the aligned fibers were secured to a metal strip.

After both ends were fabricated as outlined above, the whole array was affixed to a metal support plate.

**Polishing and finishing.** The two dimensional end of the array was polished with successively finer grit of polishing paper (3M; 180, 220, 400, and 600 grit sanding papers) until it was flush with the ST connector tip. The one dimensional end fibers were then cut using ordinary scissors and polished using a Fibrmet® optical fiber polisher (Buehler) equipped with 3 µm and 0.3 µm grit aluminum oxide disks.

## Summary 1.

### Software for rapid multispectral deconvolution.

To correct for vignetting, tilt/curvature of the array, and to calibrate the system in terms of wavelength and pixel positions, reference images are obtained prior to sample acquisition.

**Vignetting.** When optical lenses are placed in series, as they are in our spectrograph, a larger accepted cone of light comes from on-axis object points than from those that are off-axis, a phenomenon known as *vignetting*. This occurrence is evident in our ICCD images of the linear end of the fiber array, e.g. casting light of equal intensity over all fibers on the 2-D end of the fiber will result in an image with the greatest intensities in the middle image rows (Figure 2A).

To correct for this, a white-light reference image is acquired by diffusing light onto a piece of white paper at the focal plane of the microscope objective. The grating is positioned so that the zero-order image of the slit (one-dimensional array end) will reach the detector. The collected image is then inverted and multiplied point for point with a sample image via software written in-house to give more emphasis to top and bottom rows and less to middle rows of the ICCD image.

**Curvature and Tilt.** A slight curve in our spectroscopic images is evident due to aberrations in the spectrograph lenses and imperfections in the array. A slight tilt in the array was also apparent when the array was not perfectly oriented parallel to the vertical axis of the ICCD chip.

To correct for this, a spectroscopic reference image such as that obtained for wavelength calibration (see below) is first acquired. Our software then corrects for these imaging errors by fitting a third-order polynomial to the pixels with the greatest intensity within a range of user-defined pixel values corresponding to the positions that encompass the parabolic reference atomic line in another reference image. The program then rotates



the rows of subsequently acquired spectroscopic images left or right to align them within one horizontal pixel. Figure 2B shows the image in Figure 2A corrected for vignetting and curvature.

**Calibration of Wavelengths.** To calibrate each image according to wavelength, a first-order image of the radiation from a calibration lamp (i.e., a mercury lamp) is obtained. This generates an image with a series of bright vertical bands corresponding to atomic emission lines. Extraction of a single row of pixels provides a spectrum of the calibration lamp that can be used to calibrate the entire image. In addition, this image can be used as a default standard for curvature correction to subsequent sample images.

**Selection of Ribbon Start to End Positions.** During assembly of the linear array end, it was often the case that a small space would separate adjacent fibers due to construction errors. The result is regions of unused rows of pixels in the CCD camera images. To extract only those areas which contain useful optical information to be used in the reconstructed images, pixel start/end position values have to be entered into the computer program so that light from each fiber is properly registered.

The reference images used for vignetting correction can also be used to determine the approximate starting and ending pixel position values for each fiber ribbon. Dramatic changes in intensity are evident in the image indicating the approximate start/end pixel position values. These preliminary values are entered into the program and reconstructed images are generated subsequently. An image of an object with distinct boundaries such as the letter "A" in Figure 3 must be acquired to "fine-tune" the pixel values. Figure 3C shows a reconstructed zero-order gray-scale image of the letter "A" found in Figure 3A, demonstrating the level of image fidelity we have been able to achieve with our experimental set-up. Figure 3B is a "blurred" image of Figure 3A showing the amount of image fidelity that would be expected for our system. The image was created by sectioning Figure 3A into 17 x 32 blocks (consistent with the dimensions of our array) and using the average intensities value of each block to recreate the image.

**Concept.** Once an ICCD image is obtained, software is used to extract the spatial and spectral information embedded in the image. Each image is essentially a two dimensional intensity map of fiber position (vertical pixel axis) and wavelength (horizontal pixel axis). In the ideal case of perfect 1:1 registration between array fibers and ICCD rows, each row in the image could be extracted to produce a spectrum corresponding to an individual fiber, and each column in the image could be treated as the monochromatic intensities of all the fibers. Unavoidable problems such as vignetting from the optics in the spectrograph, uncorrected tilts in the array, and imperfect registry of the array with the detector pixels prevent this ideal situation from being realized. All these problems can be, and are, corrected in software, in addition to performing the complete image reconstruction and display.

**Flow diagram of software.** Software was written for image reconstruction with the use of Labview<sup>®</sup> 4.1 (National Instruments) augmented by IMAQ<sup>™</sup> Vision virtual instruments for Labview<sup>®</sup> 4.1 (National Instruments). The simplest version software allows the user to choose wavelength(s) to reconstruct the image. To reconstruct wavelength(s), the program first prompts the user to load an image file. Software corrects for curvature of the spectra, tilt of the array, and vignetting of the image within limits, and makes it unnecessary to exactly fit 544 fiber images onto 544 vertical pixels. To select the wavelength(s) to be reconstructed, the user is prompted for the vignetting-

corrected image file. The user is then given the option of selecting a wavelength (column of the image) to be assigned to red, green, and/or blue of a RGB color image. To reconstruct the images at user-selected wavelengths, the user is prompted to enter starting and ending pixel row values for each of the 17 ribbons. On the basis of the number of pixels occupied by the array on the CCD chip, the image pixels are linearly interpolated to span 32 image points for image fiber ribbon. The program then cuts and reorders the one dimensional data array according to the ordering of the rows of the fiber array for each of the red, green, and blue color value arrays.

**Univariate Data Treatment.** For methods in which the spatial distribution of a single wavelength or a combination of wavelengths is desired, for instance the spatial distribution of one or several atomic lines during the development of a laser-induced spark, a single column or several columns can be extracted from the image and reconstructed. To do this, a single CCD column or several CCD column are extracted, multiplied by the inverted intensities of a white-light reference image, and cut and re-ordered into the proper spatial arrangement.

Figure 4 shows a first-order reconstructed gray-scale intensity image of the 722.9 nm emission line of lead generated from a single column of an ICCD image. A lead target was placed at the focal plane of the objective lens which was subsequently ablated with a Surelite I Nd:YAG laser (Continuum). A programmable pulse generator (Princeton Instruments, Inc., Model PG-200) was used to gate the ICCD. The Nd:YAG laser provided a trigger for gating the detector. The PG-200 provided a delay of 1.8  $\mu$ s from the onset of the trigger with a 200 ns time window for imaging.

A number of treatments of the spectroscopic data are implemented in software to enhance the chemical imaging capability of the system. These treatments fall into two broad categories: (a) pattern recognition and (b) false-color rendering.

**Pattern Recognition.** To utilize the array described here to its fullest potential as a spectroscopic pattern-imaging system, we treat the rows of the CCD images as spectra and perform principal component analysis (PCA) on the entire image.

PCA,<sup>1-5</sup> a multivariate dimension reduction method, takes  $m$  spectra with  $n$  independent variables (e.g., detector channels) and produces a new set of orthogonal eigenvectors (or plotting axes) that are linear combinations of the original variables. The predominant axis, termed principal component one (PC1) describes the greatest variability in the data set. Subsequent PCs, ranked in decreasing eigenvalue, describes successively less variability until only noise is being accounted for. Since adjacent rows on the CCD image (e.g., spectra) are highly correlated with one another, generally the first few PCs will describe over 95% of the variability in the data, making its interpretation simpler.

The direct product of these PC vectors with the sequence of  $n$  rows in an image produces a vector with  $n$  values with intensities based on the score of each PC as a function of position. The values can then be cut and reordered in the same manner as the univariate reconstructions forming an image that highlights physical and/or chemical variation as determined by PCA across the sampled region.

The PCA performed by our software is accomplished by singular value decomposition (SVD).<sup>6</sup> SVD is a computational method that simultaneously calculates the column-mode eigenvectors, row-mode eigenvectors (PC loadings), and the singular values (eigenvalues) of a data matrix according to the equation

$$A = USV^T \quad (4)$$

where  $A$  is the data matrix (CCD image),  $U$  contains the column-mode eigenvectors of  $A$ , the diagonal of  $S$  contains the square roots of the eigenvalues of  $A$ , and  $V$  contains the row-mode eigenvectors (PC loadings) of  $A$ . The set of column-mode eigenvectors in  $U$  and the row-mode eigenvectors in  $V$  are orthogonal. The values in the diagonal of  $S$  are proportional to the amount of variance that each describes.

Our software performs PCA using Labview's Singular Value Decomposition V.i., for example, which produces three orthogonal matrices: an  $n \times n$  matrix whose diagonal contains the eigenvalues generated in the singular value decomposition in decreasing order, an  $n \times n$  matrix containing the principal component vectors, and an  $m \times n$  matrix containing the scores on each PC, where  $m$  is the number of rows (spectral domain) in the image and  $n$  is the number of columns (wavelength domain) in the image. PCA is a multivariate method which takes into account the variation in the intensity of the radiation over a range of wavelengths as defined by the experiment rather than just one or a few wavelengths. It has the unique advantage of modeling statistically significant variation while suppressing random measurement error in a data set. PCA enables us to extract the relevant information in the first few PCs and ignore the random noise in the subsequent PCs.

**ITTFA.** Unfortunately, the principal component model is often abstract and an image based on PCA scores is not a direct chemical mapping of a sample, although it is related to such a map by coordinate rotation. Target transformation algorithms<sup>6-9</sup> rotate the principal components until all the factors are positive while still spanning the original factor space.

Transformations are carried out by finding a transformation matrix,  $M$ , such that

$$C_{pred} = UM \quad (5)$$

where  $C_{pred}$  is the prediction of the new coordinate system. The eigenvectors  $E_{pred}$  of the new coordinate system can be found from the inverse of  $M$ :

$$E_{pred} = M^{-1}SV^T \quad (6)$$

The original data matrix,  $A$ , is related to  $C_{pred}$  and  $E_{pred}$  via:

$$A = C_{pred} E_{pred} \quad (7)$$

By substituting equations 2 and 3, equations 5 through 8 show how the rotated factors are related to the unrotated factors.

$$A = (UM)(M^{-1}SV^T) \quad (8)$$

$$A = U(MM^{-1})SV^T \quad (9)$$

$$A = UISV^T \quad (10)$$

$$A = USV^T \quad (11)$$

Iterative target-transformation factor analysis (ITTFA),<sup>10-12</sup> one such target transformation algorithm, is a self-modeling curve resolution method that mathematically resolves overlapping or independent spectral contributors in a data matrix. ITTFA modifies test vectors in an iterative fashion until estimates of the composition profiles are non-negative. This, in effect, causes the abstract PCs to be transformed to profiles that correspond to real chemical or physical properties of the sample (see for example reference 25).

**False-color imaging.** Simultaneous visualization of more than one pattern in a reconstructed image can be achieved by assigning red, green, and blue color values for up to three different components. In the following discussion we refer to example images acquired of a laser breakdown plume generated from a lead sample. When using more than one wavelength, the intensities associated with lead atomic emission, for instance, at 722.9, nitrogen atomic emission at 746.8 nm, and sodium atomic emission at 589.6 nm can be assigned to red, green, and blue false-color values, respectively. A system could be arranged to produce near-real-time images of the color-coded spatial distribution of the three wavelengths. By mapping the scores of one or more PCs on the spectra as a function of position resulting from PCA analysis, or by mapping the predicted column profiles resulting from the rotated factor model from ITTFA for each CCD image, a false-color RGB map can be created in much the same way reconstructed wavelength mapping is done. For instance, the score on PC1 (or predicted column profile from the first factor from ITTFA) could be assigned red false-color values. Subsequent PCs or column profile factors could be assigned green and blue false-color values.

### **Summary 3.**

#### **Multidimensional Fluorescence**

Figures 5a and 5b are schematics of the imaging spectrofluorometer. Figure 5a illustrates the spatial relationship between the condensing optics of the lamp and the excitation spectrograph. UV excitation was provided by an Oriel model 66021 high-pressure 1000W Hg(Xe) short-arc lamp with a synthetic fused-silica envelope. This light source produced broad and intense Hg emission lines within the range of 250 nm to 600 nm which augment the continuum output (300 nm to 800 nm) of the Xenon fill gas. Radiation from the arc was collected by a two-element condenser, focused by an F/3 lens, and reflected 90° by a plane mirror onto the entrance slit of an ISA/Jobin-Yvon model CP200 F/2.9, 0.190 m imaging spectrograph. The dispersive element of the CP200 was a concave holographic grating with 200 grooves/mm having a groove modulation suitable for use in the ultraviolet. This combination produced a linear dispersion of 25.2 nm/mm in its focal plane. A spatial filter in the form of a plastic mask was used for rejection of excitation radiation other than ultraviolet light in the first grating order. The spectrograph was turned 90° onto its side, such that the source was dispersed vertically instead of horizontally. This arrangement directed shorter wavelengths nearer the top of a cuvette positioned such that the focal plane of the CP200 was located at one of the corners (upper left with reference to Figure 5b) of the cuvette, minimizing the distances traversed through the sample by the excitation radiation to its focus and by the fluorescence along the collection axis. The center of the excitation wavelength interval could be shifted by raising or lowering the entire spectrograph, which was mounted on a vertical-translation stage for this purpose.

Fluorescence from the sample was collected and collimated at 90° with respect to the excitation axis by an F/4 plano-convex lens, then focused at the slit of a second imaging spectrograph by another identical lens; the collection axis was aligned in the excitation focal plane. The emission-wavelength sorter was a Spex model 270M 0.270 m, F/4 Czerny/Turner-configuration device utilizing a ruled plane grating with 300 grooves/mm, blazed at 300 nm. The grating was mounted on a turret which, through its

rotation, allowed for selection of the center of the emission wavelength interval. All refractive optics in the instrument were made of UV-grade synthetic fused silica. Collection of fluorescence using these chromatic lens elements limits the range of wavelengths within the EEM over which a satisfactory focus can be simultaneously obtained. This limitation exists because the dispersion by the lens material increases rapidly with decreasing ultraviolet wavelength. The use of reflective, instead of refractive, optics would eliminate this aberration; however, these were not implemented during this work.

Signal detection was via a Santa Barbara Instrument Group model ST-6 thermoelectrically-cooled CCD camera.<sup>13</sup> The active area of the Texas Instruments TC241 CCD used in the ST-6 is 8.6 mm wide and 6.5 mm high containing 750 X 242 pixels, each of which is 11.5\_μm X 27\_μm in area. The camera housing had been modified for enhanced UV throughput by removing a protective glass cover from the array, and by replacing the 2.5 cm-diameter glass window with one made of synthetic fused silica. A water jacket constructed from copper tubing had also been fitted to the housing of the CCD in order to improve heat flow from the normally air-cooled sinks in thermal contact with the TEC. This latter modification allowed the array to be operated at a minimum of -42\_C, using a pump to circulate water from an ice bath through the jacket. The active area of the CCD and the linear dispersions of the spectrographs combine to produce an EEM which covers approximately 115 nm in the excitation space and 105 nm in the emission space.

**Theory.** With three-dimensional data structures, such as collections of EEM's, complete analyte selectivity can be achieved by mathematical separation of the analyte signal from the signal of the complex background. One method of accomplishing this separation is by employing a parallel factor analysis (PARAFAC) model to decompose the collection of EEM's into the spectral profiles of the pure component species. The PARAFAC decomposition exploits the uniqueness properties<sup>12</sup> intrinsic to collections of EEM's and other types of data with 'bilinear' structures. An EEM of a pure compound is considered 'bilinear' as it can be expressed as a scaled outer product of two column vectors: **x**, the excitation profile of the compound at any one emission wavelength, and **y**, the emission profile of the compound at a single excitation wavelength. That is, the EEM of a pure compound, **R**, is

$$\mathbf{R} = \hat{\mathbf{x}}\hat{\mathbf{y}}^T + \mathbf{E} \quad (1a)$$

or equivalently

$$R_{i,j} = \hat{x}_i\hat{y}_j + E_{i,j} \quad (1b)$$

where the superscript T indicates the transpose of a matrix and the subscripts *i* and *j* indicate the *i*th excitation wavelength and the *j*th emission wavelength, respectively. The symbol ^ indicates the estimate of a true spectrum, while the matrix **E** is the collection of random errors associated with any measurement. The EEM of the analyte is linear with respect to the excitation and emission profiles, hence 'bilinear'.

In the cases of multiple fluorescent species in a sample, the bilinear model of  $\mathbf{R}$  can be generalized. Here  $\mathbf{R}$ , assuming linear additivity of signal, is the sum of  $N$  'pure' EEM's collected at the appropriate concentrations. Hence,

$$\mathbf{R} = \sum_{n=1}^N \hat{\mathbf{x}}_n \hat{\mathbf{y}}_n^T + \mathbf{E} = \hat{\mathbf{X}} \hat{\mathbf{Y}}^T + \mathbf{E} \quad (2a)$$

or equivalently

$$R_{i,j} = \sum_{n=1}^N \hat{X}_{i,n} \hat{Y}_{j,n} + E_{i,j} \quad (2b)$$

where the  $N$  columns of the matrices  $\hat{\mathbf{X}}$  and  $\hat{\mathbf{Y}}$ , individually designated  $\hat{\mathbf{x}}_n$  and  $\hat{\mathbf{y}}_n$ , represent the 'pure' excitation and emission spectra of the  $N$  fluorescent species in  $\mathbf{R}$ . Equations 2a and 2b can be further generalized for multiple samples,  $\mathbf{R}$ , where  $\mathbf{R}$  is an  $I \times J \times K$  tensor with the index  $k$  designating the sample number. The EEM of the  $k$ th sample in a multiple component mixture can be generalized to

$$\mathbf{R}_k = \hat{\mathbf{X}}(\hat{\mathbf{Z}}_{k,*} \mathbf{I}) \hat{\mathbf{Y}}^T + \mathbf{E}_k \quad (3a)$$

or equivalently each element in the tensor  $\mathbf{R}$  is assumed to follow the model

$$R_{i,j,k} = \sum_{n=1}^N \hat{X}_{i,n} \hat{Y}_{j,n} \hat{Z}_{k,n} + E_{i,j,k} \quad (3b)$$

Here  $\hat{\mathbf{Z}}$  is a  $K \times N$  matrix with the  $n$ th column consisting of the relative concentrations of the  $n$ th compound throughout the  $K$  samples. The subscript ' $k,*$ ' in equation 3a indicates the  $k$ th row, all columns, of the matrix, and  $\mathbf{I}$  is the identity matrix.

The PARAFAC based decomposition of  $\mathbf{R}$  into estimates of the excitation and emission profiles,  $\hat{\mathbf{X}}$  and  $\hat{\mathbf{Y}}$ , and relative concentrations,  $\hat{\mathbf{Z}}$ , is unique to a scalar multiple of each column in  $\hat{\mathbf{Z}}$ .<sup>14</sup> The PARAFAC decomposition can be employed to deconvolute highly overlapping spectra in EEM's collected from multiple mixtures. This permits removal of instrumental backgrounds and estimation of the number and distribution of fluorescent components in a collection of samples.<sup>15-16</sup>

The decomposition can be used to predict analyte concentration for unknowns when one or more samples is of known analyte concentration. Since  $\hat{\mathbf{Z}}$  is unbiased by the presence of uncontrolled spectral interferents in the analytic samples, the accurate prediction of analyte concentration can be accomplished in the presence of spectral interferences that are not included in the calibration set.<sup>16,17</sup> This predictive asset is absent in univariate and multivariate calibration.<sup>17</sup> The performance of this instrument during EEM production and subsequent analysis of these EEM's by the PARAFAC model for calibration is the theme of a separate paper not covered in this report.<sup>18</sup>

**Measurements.** A 5 mg/mL standard solution of naphthalene in ethanol was prepared by dissolving 0.500g of scintillation-grade naphthalene crystals (99+%, Aldrich) in anhydrous ethyl alcohol (Quantum) in a 100 mL volumetric flask. A 10 parts-per-million (ppm) stock solution of naphthalene in sea water was made by adding 4.00 mL of the naphthalene/ethanol solution to ocean water rapidly stirring in a 2 L volumetric flask, then filling to the mark with ocean water. Ocean water was obtained from the Baruch Marine Science Institute, located on the north inlet of Winyah Bay near Georgetown, SC, and was not pre-treated in any way. This stock solution was diluted with ocean water to produce eleven naphthalene/water standards of concentrations between 28 and 2000 parts-per-billion (ppb). A one ppm ( $\mu\text{L/mL}$ ) stock solution of styrene (99%, Aldrich) in ocean water was made by diluting 2.00 mL of styrene with the latter in a 2000 mL volumetric flask. Styrene standards ranging from 5 to 1000 ppb in ocean water were produced from this styrene stock.

EEM spectra were taken of the eleven naphthalene/ocean water standards, the styrene/ocean water standards, and several ocean water blanks using the imaging spectrofluorometer described above. The arc lamp was thermally stabilized by operation at approximately one kW for a minimum of thirty minutes before any data was collected. The CCD detector was maintained at  $-41^{\circ}\text{C}$ , and the entrance slit of the excitation spectrograph and that of the emission spectrograph were set at 0.25 mm and 0.100 mm, respectively. The emission wavelength range was centered at 340 nm for naphthalene and at 300 nm for styrene. Each standard and blank was exposed for 60 seconds; a "dark frame", or baseline EEM, was also collected over this time interval. Samples were contained in square-cross-section, UV-grade fused silica fluorescence cuvettes of 3.5 mL internal volume. Cuvettes were flushed thoroughly with ocean water between samples, and were rinsed with each sample before being filled.

**Data Pretreatment** EEM's were collected and stored in the "low resolution" mode (bins three pixels vertically and two pixels horizontally) of the CCD operating software, in order to decrease the time required for digitization and downloading of images, and to improve the signal-to-noise. Each image was stored as a double-precision SBIG ASCII file.<sup>19</sup> These data files were then converted to double-precision ASCII files by a C++ program written in this laboratory. This conversion produced a  $250 \times 121$  element matrix per sample. Each of these elements spanned 0.4 nm in the excitation domain and 0.9 nm in the emission domain. The actual wavelength range of each pixel varies slightly with the wavelength and center position of each spectrograph.

After conversion of the data files, each image was dark-count-subtracted, normalized to correct for the wavelength dependence of both the source radiance and the throughput efficiency of the excitation optics, and compressed to an  $80 \times 60$  element matrix. All post-collection data processing was performed in the Matlab (MathWorks, Inc., Natick, MA) operating environment on Gateway P5-90 personal computers (Gateway2000, E. Sioux Falls, SD). Data compression (3:1 em ; 2:1 ex) was performed to increase data processing speed. Each element in the compressed EEM spans 1.2 nm in the excitation domain and 1.8 nm in the emission domain. This is comparable to the calculated resolution of the spectrofluorometer.

A dark frame was used to correct the EEM's for the thermal background signal from the detector. Although the dark-count baseline could be incorporated in the PARAFAC model, its removal prior to lamp-intensity correction is essential for

determining the apparent lamp intensity profile. The lamp intensity correction was employed to permit determination of excitation profiles that are independent of the substantial variance in the radiance of the source over the range of excitation wavelengths in the EEM's. Moreover, this type of correction has the added benefit of weighting each element in the predicted excitation profiles based on the relative efficiency at a particular excitation wavelength, instead of on the convolution of the fluorescence excitation efficiency and spectral irradiance of the sample. The lamp intensity profile was estimated by ratioing the UV-absorbance spectrum of fluorescein to its excitation profile as measured by the EEM spectrofluorometer. This yielded a vector of weights, the reciprocal of the lamp intensity profile, which was used to scale the  $J$  emission profiles in each EEM (Figure 6). No correction for the wavelength-dependent efficiencies of the detector and the collection optics or for the variation in pixel response across the detector was attempted because the effects of these on the EEM's were nominal compared to the effects of the varying spectral irradiance. It was unnecessary to produce perfectly corrected EEM's for quantitative purposes; thus, only the minimum amount of data pre-processing necessary to provide reasonable precision in the results was performed.

**Profile Estimation..** The excitation/emission/concentration profiles in equations 3a and 3b were estimated by a version of the TUCKALS3 alternating least squares algorithm<sup>11,20</sup> that has been constrained to minimize the error in decomposing  $\mathbf{R}$  based on the PARAFAC model. Termination of the alternating least squares approximation sequence was based on the unconstrained correlation coefficient criterion.<sup>21</sup> Extra constraints, such as non-negativity or unimodality, could be imposed on the estimated excitation and emission profiles; however, this was not done under the belief that the data should "speak for itself."

Two validation tools were employed to check the sufficiency of the PARAFAC decomposition to model the data. Analysis of the magnitude and distribution of the elements in the residual matrix,  $\mathbf{E}$ , was first employed. When the appropriate number of factors is included in the model, inclusion of an additional factor will not significantly improve the fit of the model to the data. Similarly, when the appropriate number of factors is included in the model, the errors,  $\mathbf{E}$ , should present no topological trend when plotted as an EEM. A trend would be evident if one-too-few factors were incorporated in the model. Finally,  $\hat{\mathbf{X}}$ ,  $\hat{\mathbf{Y}}$ , and  $\hat{\mathbf{Z}}$  were visually inspected to determine if they made chemical sense.

**Instrumental Background Subtraction.** A typical spectrofluorometer minimizes stray excitation light through the use of a long-pass filter. Such a rejection element cannot effectively serve as part of a system in which broadband excitation and emission occur simultaneously, because of the overlap of excitation radiation and fluorescence of the same wavelength. Therefore, EEM's produced by this type of instrument are characterized by a convolution of the fluorescence spectrum of the sample with a background containing, in addition to typical Stokes-shifted components, comparatively intense elastically-scattered and other stray excitation radiation transmitted by the emission optics.

By employing a holistic approach to the use of the imaging spectrofluorometer with multidimensional EEM deconvolution, however, the detrimental effects of a changing background signal are controlled, and the elastic-scattering component of this



background can be used as an internal wavelength reference. Figure 7 shows a negative image of the background obtained using distilled water as a blank. The elastic-scattering portion of this signal manifests itself as a diagonal across the EEM corresponding to equal energy values on the excitation and emission axes. The more intense Hg lines at 254 nm, 313 nm, 334 nm, and 365 nm are the most prominent features along this diagonal. Other Hg lines (e.g., 280 nm and 289 nm) are less intense and, therefore, not readily visible in the figure. The background is also characterized by stray light components appearing in the images as horizontal and vertical streaks. The intensities of these striations are correlated to the intensities of the lamp lines along the diagonal. This correlation supports the conclusion that these features are primarily artifacts resulting from the effects of ruled-grating imperfections on the large amount of elastically-scattered excitation light entering the emission spectrograph. These scattering lines were not observed in EEM's of distilled water samples, were readily seen in those of ppb naphthalene/distilled water samples, and were very strong in EEM's of samples containing ocean water. This component of the background cannot be corrected by subtracting an instrumental blank, since the scattering is a function of the total species concentration and turbidity of the sample. Another component of the background is Raman scattering of lamp radiation by water. This scattering produces another diagonal – shifted to longer emission wavelengths compared to that produced by elastic scattering – the main features of which are Stokes-shifted Hg emission lines. These diagonals produced by elastic and inelastic scattering gradually diverge at longer wavelengths due to the constant energy difference between them.

Since the background varies among samples and is approximately bilinear, it can be successfully included in the PARAFAC model as an additional factor. The resolved profile of the background along the excitation axis has two main features; one corresponds to the elastic scattering of the 254 nm band, and the other is related to the more intense scattering of the 302 nm line. In this estimated background excitation profile the elastically-scattered 302 nm line is much more intense than the other bands since the EEM's were collected near the maximum of the 302 nm line. Similarly, the resolved emission profiles have two features; the first of these corresponds to the scattered 313 nm line, the second to the 334 nm line.

Although the PARAFAC model was employed to deconvolve the scattering background from the EEM's, this model is not technically correct. The interaction of the emission and excitation based Rayleigh lines follows an additive model, not the multiplicative model assumed in equations 1a and 1b. Hence, it is expected that the modeling efficiency of the background will be worse than the modeling efficiency of the naphthalene fluorescence. A plot of relative root-mean-squared-error of fit (RRMSEF), where

$$\text{RRMSEF} = \frac{\sum_{j=1}^J \sum_{i=1}^I (\mathbf{R} - \hat{\mathbf{R}})^2 \sqrt{\frac{1}{2}}}{\sum_{j=1}^J \sum_{i=1}^I (\mathbf{R})^2 \sqrt{\frac{1}{2}}} \quad (4)$$

for the PARAFAC model of equations 3a and 3b versus the percent contribution of the background to the integrated fluorescence intensity allows derivation of the modeling efficiencies of the background and naphthalene. Over the range of 20% scattering

background to 100% Rayleigh background, the graph is linear with a slope of 0.052 RRMSEF per percent increase in background contribution and an intercept of -0.0019 RRMSEF; however, at less than 20% background, the RRMSEF varies around 1%. This behavior is consistent with a system where the error of fit associated with modeling the background is 5% and the error of fit associated with modeling the naphthalene fluorescence is small compared to the inherent 1% random instrumental errors.

The effects of grating imperfections are pronounced at shorter excitation wavelengths; the background fluorescence profiles and styrene fluorescence profiles could, nonetheless, be resolved from the 19 styrene/sea water mixtures. Regression of the percent background contribution against the RRMSEF yields an 18% RRMSEF associated with the background and a 5% RRMSEF associated with styrene. Nevertheless, meaningful estimates of the excitation and emission profiles were still obtained. In the estimated excitation profile, the shoulder of the intense Rayleigh region is evident between 210 nm and 260 nm. Also evident is a feature associated with the 280 nm lamp line. In the emission profile, the 280 nm, 289 nm, 296/302 nm, 313 nm, and 334 nm Rayleigh lines are clearly evident. It is shown below that accurate calibration was performed in spite of these small model errors associated with the background signal.

#### Summary 4.

#### Solid-State Optical Computation of Spectroscopic Properties

The fundamental mathematical operation that characterizes prediction of properties via regression from optical spectra is the calculation of the direct product between the spectrum and a predetermined regression vector. Following this process, the scalar result is scaled appropriately and offset to correspond to the basis from which the regression vector was derived.

Calculation of the direct product is accomplished as a series of simple wavelength-dependent signed multiplications followed by summation of all the signed terms. In commercially-available instruments meant for this purpose, a dispersive element of some sort disperses the spectrum of the analyte, a detector records the wavelength-dependent signal strength and converts it to a digital signal, and the calculation of the direct product is performed by the CPU of a computer. However, all of the elemental steps of this procedure have optical analogs.

For example, unsigned multiplication by a factor less than one can be accomplished by the simplest of optical computation methods, namely that of shadowcasting. In shadowcasting, light at wavelength  $\lambda$  of intensity  $I_o(\lambda)$  is passed through a partially transparent filter of transmittance  $T(\lambda)$ . The intensity of the transmitted light is then  $I_o(\lambda) \cdot T(\lambda)$ . Similarly, the act of summation over all wavelengths is accomplished implicitly by directing all the light of different wavelengths onto the same optical detector, producing a signal proportional to the sum of all detected photons. In principal, since multiplication and summation are both readily accomplished with a simple optical process, it should be possible to process multiwavelength spectra by passing the multiwavelength light, without dispersion, through a filtering mask with wavelength-dependent transmittance factors onto a common detector. We leave the question of the manufacturability of such a mask for a later discussion in this manuscript.

If we assume that multiwavelength shadowcasting masks as described above can be prepared, two complications arise that could prevent this simple idea from being realized. First and most significant is that the individual results of multiplication in the necessary direct product are signed, while those from shadowcasting are unsigned. However, since optical spectra are non-negative, negation only occurs in the regression vector. We are therefore free to separate the positive and negative lobes from one another into two separate masks. The first mask need only have transmittances that are similar to the regression vector's positive lobe, with zero transmittance at any wavelength at which the regression vector is negative. The second mask would similarly have transmittances reflective of the absolute value of the negative portions of the regression vector, with zero transmittance where the vector is positive. Two separate summations via simultaneous detection of these positive and negative components can then be performed, and a simple electronic circuit used to invert the negative result and add the two signals together. Equivalently, a "position sensitive detector" (PSD) can be used that implicitly provides an output that is the difference of two signals.

The second complication to this optical approach to multivariate prediction is that of scaling. Regression vectors are not selected appropriately for this optical method by standard procedures. As a typical example, the regression vector used in reference 1 has a maximum positive value of 0.000528, and a maximum negative value of -0.000336. Shadowcasting filters with maximum transmittances of 0.0528% and 0.0336% could be used to mimic this regression vector, but only with a severe loss of detectable signal and poor signal to noise. Best S/N performance can be expected with the greatest possible signal; therefore we may choose to produce shadowcasting filters in two different ways, depending on the detector type. If two separate detectors are used with appropriate amplifier circuitry for rescaling, the filters may each have maximum transmittances of 1, with transmittances at all other wavelengths than the maximum for each filter scaled appropriately, treating each lobe independently. If, on the other hand, a PSD-type detection system is used then only a single electronic scaling factor is possible, and the two filters must be scaled together relative to the maximum absolute value of the regression vector. In either case, the fact that the standard approach to computational prediction requires scaling after the calculation of a direct product frees us to select any arbitrary scaling factor for the shadowcasting mask transmittances, provided that the reciprocal of this factor is then incorporated into the scaling factor used to convert the electronic signal into a usable numeric value.

If we compare the operation of the system described above to the conventional approach to predictive spectroscopy, the most obvious differences between the two are the lack of dispersive elements and a digital computer in the optical computation method. The mathematical operations underlying the prediction are being performed by a simple form of optical computing, rendering the digital computer unnecessary. The remaining elements for amplifying and presenting the result are little different from those that might be used in a pH meter, for example.

## List of Publications and Reports

Single-Measurement Excitation/Emission Matrix Spectrofluorometer for Determination of Hydrocarbons in Ocean Water 1. Instrumentation and Background Correction

A.R. Muroski, K.S. Booksh and M.L. Myrick

Anal. Chem. 68(1996), 2524.

Single-Measurement Excitation/Emission Matrix Spectrofluorometer for Determination of Hydrocarbons in Ocean Water 2. Calibration and Quantitation of Naphthalene and Styrene

K.S. Booksh, A.R. Muroski and M.L. Myrick

Anal. Chem. 68(1996), 3539.

Multivariate Optical Computation for Predictive Spectroscopy

M.P. Nelson and M.L. Myrick

Anal. Chem. 70(1998), 73.

Single-Shot Multiwavelength Imaging of Laser Plumes

M.P. Nelson, W.C. Bell, M.L. McLester, and M.L. Myrick

Appl. Spectrosc. 52(1998), 179.

Design of Thin Film Filters for the Monitoring of Chemical Reactions

J.A. Dobrowolski, P.G. Verly, J.F. Aust, M.P. Nelson and M.L. Myrick

in Proceedings of the SPIE Annual Meeting on Optical Science and Engineering, San Diego, California, July, 1997, 232..

Single-Shot and Multiwavelength Imaging of Laser Plumes

M.P. Nelson and M.L. Myrick

Proc. SPIE-Int. Soc. Opt. Eng. (1998), 3261(Three-Dimensional and Multidimensional Microscopy: Image Acquisition and Processing V) 232-243.

Multivariate Optical Computation for Predictive Spectroscopy

M.P. Nelson, J.F. Aust, J.A. Dobrowolski, P.G. Verly, and M.L. Myrick

Proc. SPIE-Int. Soc. Opt. Eng. (1998), 3261(Three-Dimensional and Multidimensional Microscopy: Image Acquisition and Processing V) 232-243.

Time-dependent multivariate single-frame chemical imaging spectroscopy of laser plumes using a dimension reduction fiber optic array"

M. P. Nelson, M. L. Myrick

SPIE 3649(1999), 92.

Single-Frame Chemical Imaging. 1. Dimension Reduction Fiber-Optic Array Improvements and Application to Laser-Induced Breakdown Spectroscopy.

M.P. Nelson and M.L. Myrick

Appl. Spectrosc. (in press, 1999)

Single-Frame Chemical Imaging. 2. Chemometric Analysis and Interpretation

M.P. Nelson and M.L. Myrick

Appl. Spectrosc. (in press, 1999)

Time-Dependent Multivariate Single-Frame Chemical Imaging Spectroscopy of Laser Plumes Using and Improved Dimension Reduction Fiber-Optic Array

M.P. Nelson and M.L. Myrick

Anal. Chem. (in press, 1999)

Fabrication and Evaluation of a Dimension-Reduction Fiber-Optic System for Chemical Imaging Applications

M.P. Nelson and M.L. Myrick

Rev. Sci. Instrum. (in press, 1999)

Detection of Water-Soluble Petrochemicals by UV-induced Fluorescence

A. Muroski, M. Groner, E.L. Raleigh and M.L. Myrick

Marine Pollution Bulletin (in press, 1999)

Multianalyte Optical Sensor with High Spatial and Spectral Resolution Using a 2D to 1D Array

Maria Schiza, Susan Glenn, Matthew Nelson, Michael Myrick, S. Michael Angel

Presented at the Pittsburgh Conference, Orlando, FL, Mar 7-12, 1999.

Time-Dependent Multivariate Single-Frame Chemical Imaging Spectroscopy of Laser Plumes Using a Dimension Reduction Fiber Optic Array

Matthew Nelson, Michael Myrick

Presented at the Pittsburgh Conference, Orlando, FL, Mar 7-12, 1999.

Using Two-Dimensional Fluorescence Spectra to Determine the Origin of Water in the Congaree River in Columbia, South Carolina"

Yuan Yan, Hong Li, Michael Myrick

Presented at the Pittsburgh Conference, Orlando, FL, Mar 7-12, 1999.

Time-dependent multivariate single-frame chemical imaging spectroscopy of laser plumes using a dimension reduction fiber optic array", M. P. Nelson, M. L. Myrick, SPIE 3649(1999) (in press)

Time-Dependent Multivariate Single-Frame Chemical Imaging Spectroscopy of Laser Plumes Using an Improved Dimension Reduction Fiber Optic Array

Nelson, M. P. and Myrick, M. L.,

presented at the Federation of Analytical Spectroscopy Societies Conference, Austin, TX, October 12-15, 1998.

Single-Shot Multiwavelength Imaging of Laser Plumes

M.P. Nelson, W.C. Bell, M.L. McLester, and M.L. Myrick  
presented at Pittsburgh Conference, New Orleans, LA, Mar 1-6, 1998.

Multivariate Optical Computation for Predictive Spectroscopy  
M.L. MYrick, M.P. Nelson, J.F. Aust, J.A. Dobrowolski, and P.G. Verly  
presented at Pittsburgh Conference, New Orleans, LA, Mar 1-6, 1998.

Multivariate Optical Computation for Predictive Spectroscopy  
M.P. Nelson, J.F. Aust, K.S. Booksh and M.L. Myrick  
presented at Federation of Analytical Chemistry and Spectroscopy Societies  
Conference, Providence, RI, October 27-31, 1997

Dimensional Transformation for Imaging Spectroscopy in Near-Real-Time  
M.P. Nelson, M.L. McLester, W.C. Bell and M.L. Myrick  
presented at Federation of Analytical Chemistry and Spectroscopy Societies  
Conference, Providence, RI, October 27-31, 1997

Optical Dimension Reduction  
M.L. Myrick  
Federation of Analytical Chemistry and Spectroscopy Societies Conference,  
Kansas City, MO, September 30, 1996.

Data Analysis of Two and Three Dimensional Data Sets  
M.L. Myrick  
Federation of Analytical Chemistry and Spectroscopy Societies Conference,  
Kansas City, MO, September 30, 1996.

Eclectic Developments in Spectroscopy and Microscopy  
M.L. Myrick  
presented at NSF GOALI Workshop, Keystone, CO, Aug, 1996.

Analysis of Natural Waters by UV-Induced Excitation Emission Matrix Fluorescence  
K.S. Booksh, A.E. Fritz, M.C. Lovelace and M.L. Myrick  
presented at Pittsburgh Conference, Chicago, IL, March 3-8, 1996.

Determination of Hydrocarbons in Sea Water via UV-Induced Total Fluorescence and  
Multivariate Statistical Analysis  
A.R. Muroski, K.S. Booksh and M.L. Myrick  
presented at Pittsburgh Conference , Chicago, IL, March 3-8, 1996.

New Liquid Crystal Mask for Imaging Spectroscopy  
M.P. Nelson, M.L. McLester and M.L. Myrick  
presented at Pittsburgh Conference , Chicago, IL, March 3-8, 1996.

Distributed Sensing of Fiber-Optic Arrays  
M.P. Nelson, M.L. McLester and M.L. Myrick

presented at Pittsburgh Conference , Chicago, IL, March 3-8, 1996.

Two-Dimensional Fluorescence Spectroscopy for Hydrocarbon Detection in Water

K.S. Booksh, A.R. Muroski and M.L. Myrick

Federation of Analytical Chemistry and Spectroscopy Societies Conference,  
Cincinnati, OH, October 16-20, 1995

Total Fluorescence Spectroscopy of Aqueous Hydrocarbon Pollutants

A.R. Muroski, K.S. Booksh and M.L. Myrick

presented at Gordon Conference on Chemical Oceanography, Henniker, NH, June  
11-16, 1995

Total UV Fluorescence Spectroscopy of Aqueous Hydrocarbon Pollutants

A.R. Muroski, K.S. Booksh and M.L. Myrick

presented at Pittsburgh Conference , New Orleans, LA, March 5-10, 1995.

Detection of Dissolved Hydrocarbons in Water Using Total Fluorescence Spectroscopy

A.R. Muroski and M.L. Myrick

Federation of Analytical Chemistry and Spectroscopy Societies,  
St. Louis, MO, Oct 7-12, 1994.

Two-Dimensional Fluorescence for detection of Petrochemicals in Water

A. Muroski, E.L. Raleigh, and M.L. Myrick

presented at Pittsburgh Conference, Chicago, Ill, March 1994.

Reduction of Dimensionality Concepts for Spectroscopic and Chromatographic Data

S.L. Morgan, M. Higgins, J.F. Aust and M.L. Myrick

presented at Pittsburgh Conference, Chicago, Ill, March 1994.

### **List of Participating Scientific Personnel**

1. Allen R. Muroski (Ph.D., 1997)
2. Matthew P. Nelson (Ph.D., 1998)
3. Karl Booksh (Postdoctoral Associate, now Assistant Professor, Arizona State University)
4. J.F. Aust (Ph.D., 1996).
5. W.C. Bell (Ph.D. expected, 1999).
6. M. Groner (B.S., 1995).
7. E.L. Raleigh (B.S., 1994).



## **Inventions**

Optical encoder/decoder for smart assemblies

M.L. Myrick

(disclosed 1997)

Negative Dispersion Filter to Counteract Dispersion in Optical Fibers

M.L. Myrick

(disclosed 1997)

Erbium-doped fiber as a superfluorescent light source

M.L. Myrick

(disclosed 1997)

Model of amplifiers, etc. to model interferences

M.L. Myrick

(disclosed 1997)

Filter modifiers

M.L. Myrick

(disclosed 1997)

Hybrid Wavelength Division Multiplexing/Orthogonal Function Data transmission

M.L. Myrick

(disclosed 1997)

Data Metrics

M.L. Myrick

(disclosed 1997)

Shaping filters

M.L. Myrick

(disclosed 1997)

Spectrometer-on-a-chip

M.L. Myrick

(disclosed 1997)

ElectroOptic filters

M.L. Myrick

(disclosed 1997)

Ordering Method for NLO films

M.L. Myrick

(disclosed 1997)

Color Separation Filters

M.L. Myrick

(disclosed 1997)

ANN Input Layers

M.L. Myrick and M. Zetter

(disclosed 1997)

Hybrid Chemical/Orthogonal Methods

M.L. Myrick and M. Zetter

(disclosed 1997)

IR chemical imaging

M.L. Myrick and M. Zetter

(disclosed 1997)  
Autocorrelation Function  
M.L. Myrick  
(disclosed 1997)  
Normalization  
M.L. Myrick  
(disclosed 1997)  
Filter Simplification  
M.L. Myrick  
(disclosed 1997)  
temperature correction for optical computation devices  
M.L. Myrick  
(disclosed 1997)  
Spectrum-corrected light source  
M.L. Myrick  
(disclosed 1997)  
Optical Computation Detection for Spectroscopic Applications  
M.P. Nelson, K.S. Booksh and M.L. Myrick  
Patent Application #60/080,971 filed April 7, 1998.  
Single-Measurement 2-Dimensional Fluorometer Coupled with PARAFAC  
Decomposition  
A.R. Muroski, K.S. Booksh and M.L. Myrick  
(Disclosed, 1996)

## Bibliography

- 1 J. E. Pemberton, R. L. Sobocinski, M. A. Bryant, and D. A. Carter, *Spectroscopy*, **5**, 2 (1990).
- 2 Y. Wang and R. L. McCreery, *Anal. Chem.* **61**, 2647 (1989).
- 3 R. L. McCreery and R. T. Packard, *Anal. Chem.* **61**, 775A (1989).
- 4 H. Owen and M. Pelletier, *Laser Focus World*, **31**, 95 (1995).
- 5 J. B. Cooper, J. F. Aust, C. M. Stellman, K. Chike, and M. L. Myrick, *Spectrochim. Acta*, **50A**, 567 (1994).
- 6 E. R. Malinowski, *Factor Analysis in Chemistry* (John Wiley & Sons, New York, 1991).
- 7 J. A. de Haseth, X. Liang, and J. E. Andrews, *Anal. Chem.* **68**, 378 (1996).
- 8 L. Gao and S. Ren, *J. Auto. Chem.* **18**, 175 (1996).
- 9 P. K. Hopke, *Atmos. Environ.* **22**, 1777 (1988).
- 10 M. J. P. Gerritsen, H. Tanis, and B. G. M. Vandeginste, *Anal. Chem.* **64**, 2042 (1992).
- 11 Y. Ni, S. Kokot, and M. Hodgkinson, *Anal. Chim. Acta*, **316**, 233 (1995).
- 12 W. C. Bell, K. S. Booksh, and M. L. Myrick, *Anal. Chem.* **70**, 332 (1998).
- 13 Cooper, J. B. ; Aust, J. F. ; Stellman, C. ; Chike, C. ; Myrick, M. L. *Spectrochimica Acta*, **1994**, Vol. 50A, No. 3, pp. 567-575.
- 14 Kroonenberg, P. *Three Mode Principal Component Analysis*, DSWO Press: Leiden, **1983**.
- 15 Ferreira, M. M. C.; Brandes, M. L.; Ferreira, I. M. C.; Booksh, K. S.; Dolowy, W. C.; Gouterman, M.; Kowalski, B. R. *Applied Spectroscopy*, **1995**, *49*, 1317-1325.

- 16 Burdick, D. S.; Tu, X. M.; McGown, L. B.; Millican, D. W. *J. Chemom.* **1990**, *4*, 15-28.
- 17 Booksh, K. S.; Kowalski, B. R. *Anal. Chem.* **1994**, *66*, 782A-791A.
- 18 Booksh, K. S.; Muroski, A. R.; Myrick, M. L. Submitted to *Anal. Chem.* **1996**.
- 19 *Software Application Note*, Santa Barbara Instrument Group, Santa Barbara, CA.
- 20 Kroonenberg, P.; deLeeuw, J. *Psychometrika*, **1980**, *45*, 69-97.
- 21 Mitchell, B.C.; Burdick, D.S. *Chemom. Lab.* **1993**, *20*, 149-161.

Figure 1.

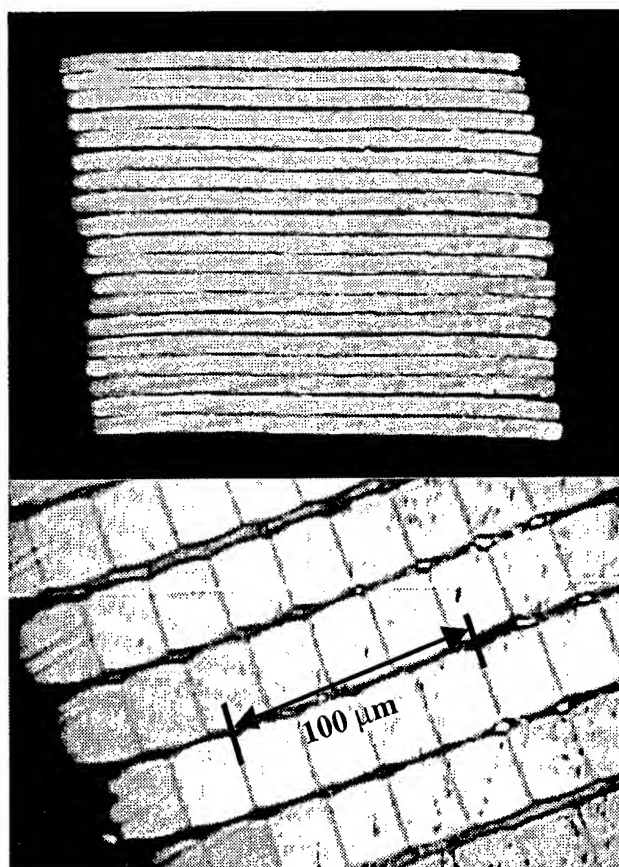


Figure 2

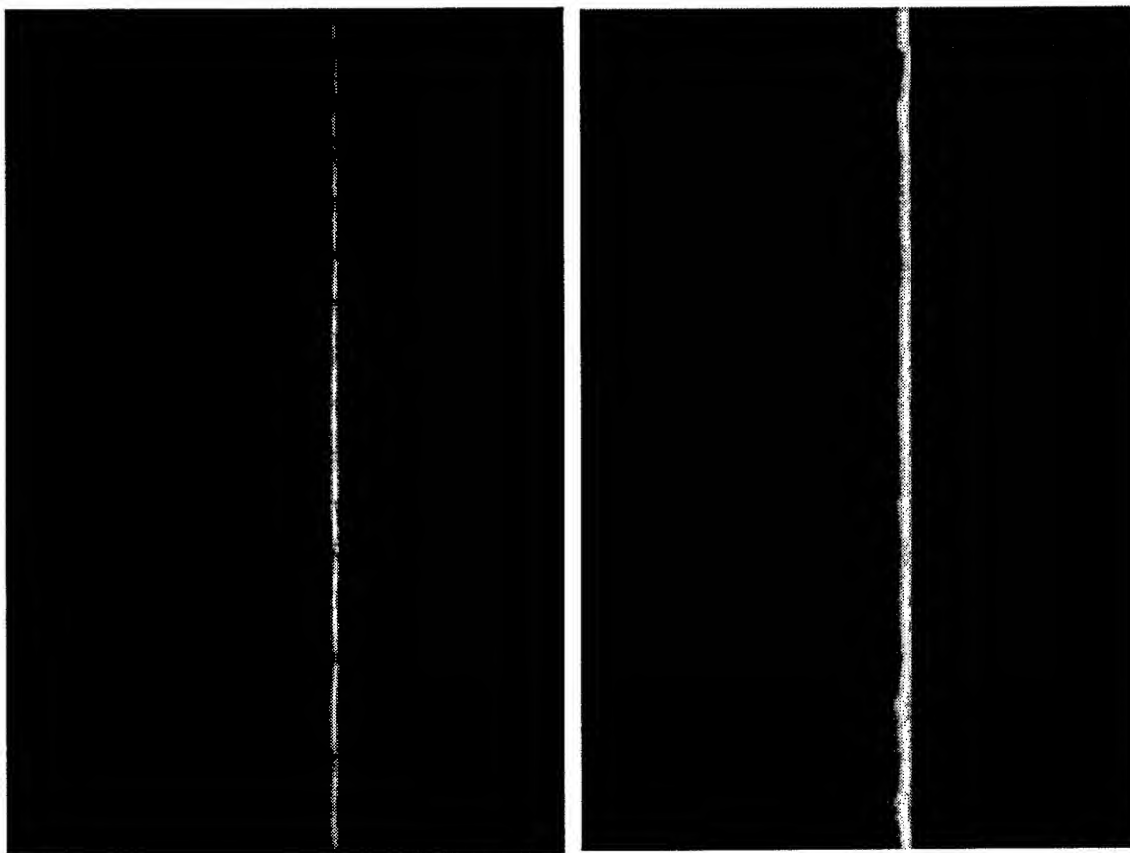


Figure 3

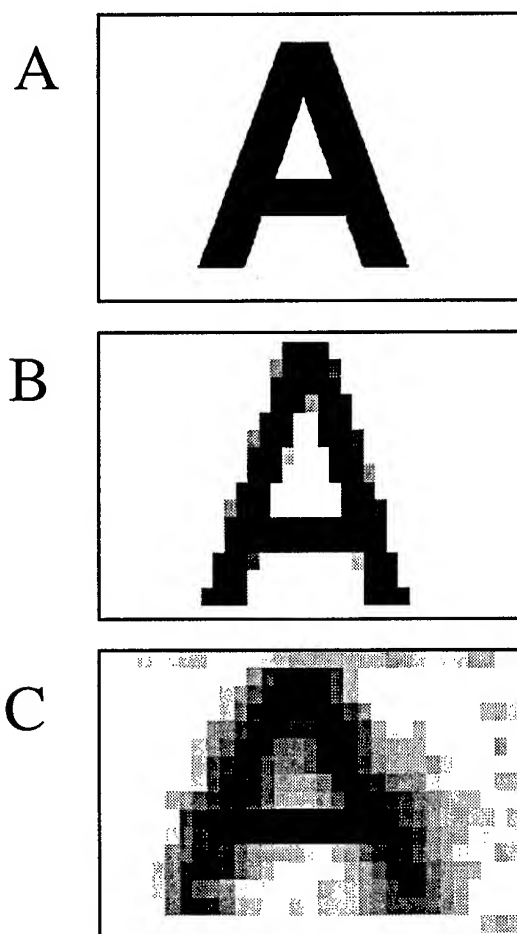


Fig4

Figure 4

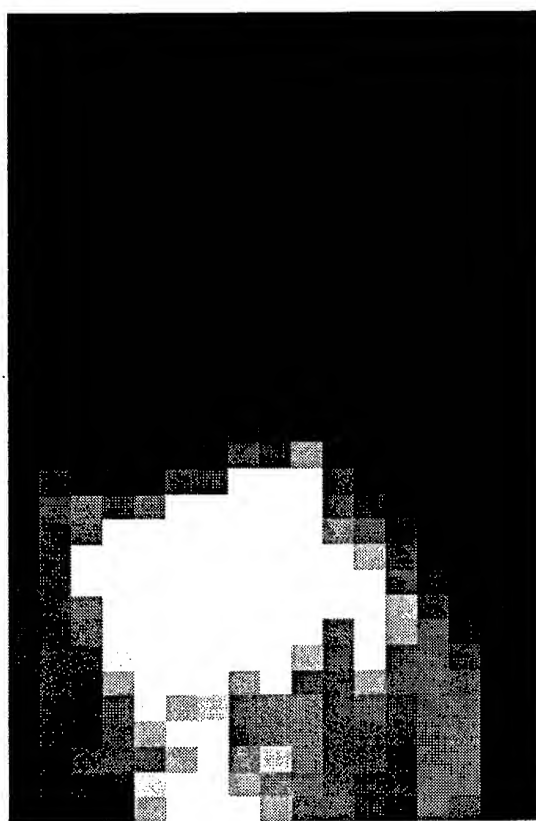




Figure 5

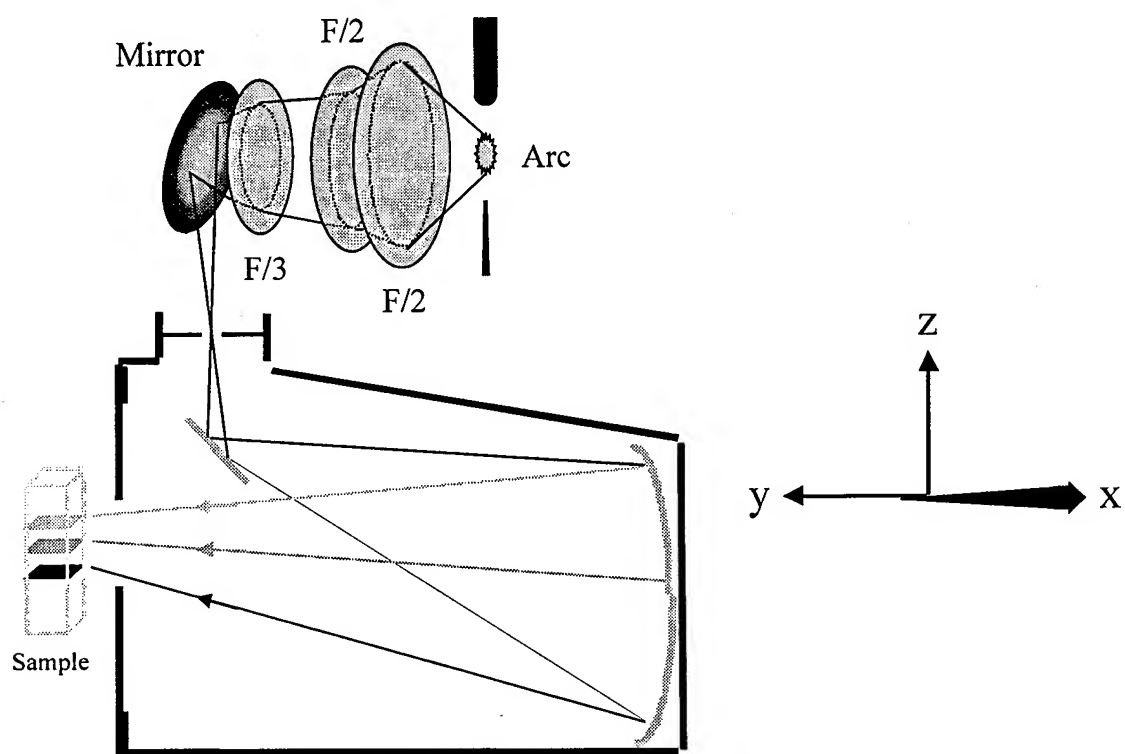


Figure 6

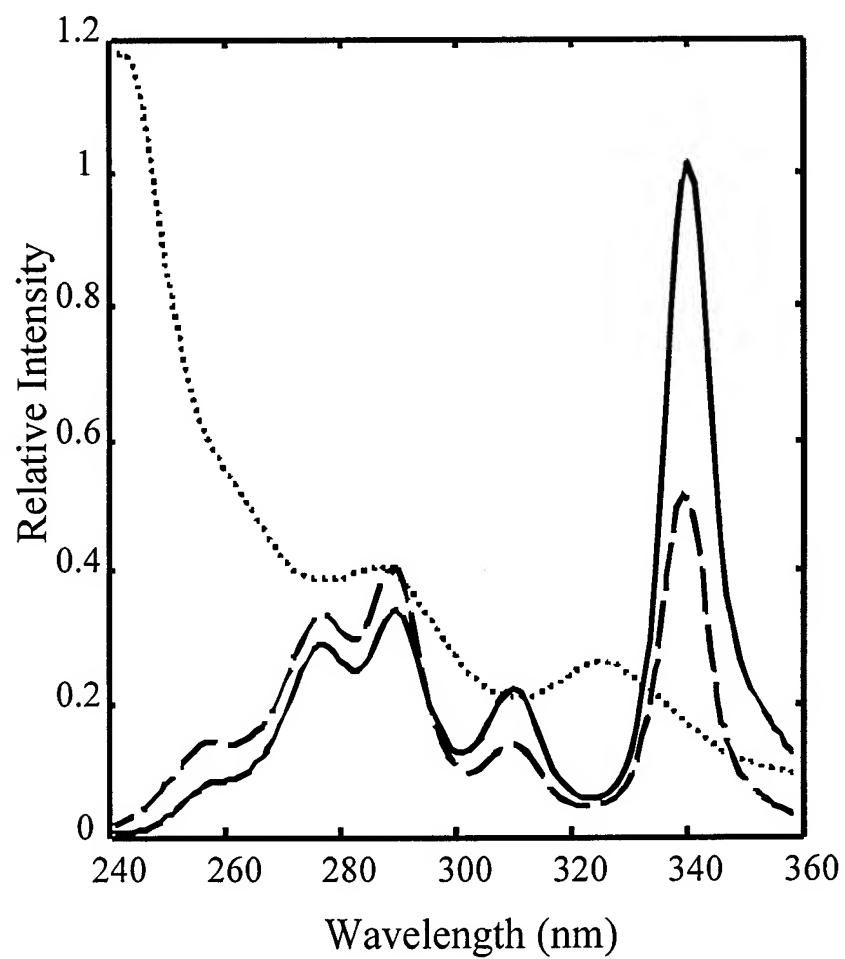


Figure 7

